Journal of The Electrochemical Society, **162** (3) A300-A307 (2015)
0013-4651/2015/162(3)/A300/8/$31.00 © The Electrochemical Society

Sea Urchin Shaped α-MnO_2/RuO_2 Mixed Oxides Nanostructure as Promising Electrocatalyst for Lithium–Oxygen Battery

Hosaeng Jang,[a] Awan Zahoor,[a] Jeong Sook Jeon,[a] Pil Kim,[a,b] Yun Sung Lee,[c,*,z] and Kee Suk Nahm[a,b,*,z]

[a]*Department of Semiconductor and Chemical Engineering, Chonbuk National University, Jeonju 561-756, Korea*
[b]*R&D Education Centre for Fuel Cell Materials & Systems, Chonbuk National University, Jeonju 561-756, Korea*
[c]*Faculty of Applied Chemical Engineering, Chonnam National University, Gwangju 500-757, Korea*

α–MnO_2/RuO_2 mixed oxides in the form of sea urchin shaped nanostructures were synthesized in the weight ratio of 82:18 *via* a simple hydrothermal method. The synthesized α–MnO_2/RuO_2 urchin nanostructure was constructed with several straight and radially grown nanorods, and composed of homogeneously distributed MnO_2 and RuO_2 nanoparticles. When the α–MnO_2/RuO_2 nanostructure was applied for air cathode catalyst, it displayed superior cyclic performances of lithium air battery with stable specific capacity, decreased overpotential and good retention rate. The α–MnO_2/RuO_2 urchin nanostructure exhibited excellent bifunctional electrocatalytic activity for oxygen reduction reaction (ORR) and oxygen evolution reaction (OER). Linear sweep voltammetry study confirmed that the α–MnO_2/RuO_2 nanostructure possesses catalytic performance comparable to that of commercial Pt/C for the ORR, while it exhibits lower onset potential and higher limiting current than those of commercial Pt/C for the OER.
 [DOI: 10.1149/2.0231503jes]

Manuscript submitted October 6, 2014; revised manuscript received December 2, 2014. Published December 16, 2014.

Lithium air battery has been considered the most promising candidate for the future power sources like electric vehicles, since theoretical energy density of the battery is about 10 times higher than that of available lithium–ion battery.[1,2] One of the critical challenges that still prevent the implementation of the Li–air batteries is the huge energy loss for achieving a reversible Li–O_2 electrochemical process. The energy loss arises from the large potential difference between the measured and the thermodynamically determined reversible potential ($E_{rev} = 2.96$ V, vs. Li/Li^+).[3,4] The discharge process of Li–O_2 batteries leads to the formation of solid Li_2O_2 on cathode surface (ORR upon discharge, O_2 (g) + 2Li+ + 2e$^-$ → Li_2O_2(s)) and the decomposition of the solid Li_2O_2 requires higher potentials during the recharge process (OER upon recharge, $Li_2O_2(s) \rightarrow 2Li+ + O_2(g) + 2e^-$).[5] In addition, sometimes by-products are also formed in the air cathode due to the reaction between electrolyte and the diffused oxygen which require further energy to be decomposed on recharge.[6] The energy loss can be suppressed by smoothing out the discharge/recharge processes based on oxygen reduction and evolution catalysts used in the air cathode.

Presently, various electrocatalysts like precious metals such as Pt, Au, Pd, Ru and metal oxides like MnO_2, Co_3O_4, CuO, Fe_3O_4 etc., are being incorporated into the carbon cathodes for lithium-air battery application.[7–9] Carbon and carbon based nanostructured materials have also been widely investigated as effective electrocatalysts for the ORR in Li–O_2 batteries.[9–12] The catalytic activity of those proposed electrocatalysts are still under discussion and their performance is far from satisfactory due to the formation of insoluble solid products. To overcome this challenge, optimization of the catalyst composition and morphology control of the catalyst and cathode materials for oxygen reduction and evolution reactions are necessary.

Manganese oxides (MnO_x) have attracted much attention because of their prominent advantages such as abundance, low cost, non–toxicity and high catalytic activity toward ORR in alkaline media.[13–15] Cao et al.[15] have studied the catalytic activities of MnO_2 with different crystalline structures to be in the sequence of β–MnO_2 < λ–MnO_2 < γ–MnO_2 < α–MnO_2 ≈ δ–MnO_2. The high catalytic activity of α–MnO_2 is attributed to the combined effect of their intrinsic tunnel (interspace in the stack of [MnO_6] octahedron) size and electrical conductivity. Moreover, nanostructured α–MnO_2, like nanospheres or nanowires, is found to exhibit superior catalytic activity due to their size and high specific surface area which can facilitate the presence of appropriate Mn_xO_y active sites at the relevant potentials to enhance ORR.[16–18] Even though α-MnO_2 has been vastly regarded as the best suitable ORR catalyst, the poor OER kinetics presents the need to explore the possibility of various other MnO_2 based bifunctional electrocatalysts. Nanostructured Mn-based oxides such as one-dimensional MnO_2 nanostructures, MnO_2–conductive matrix nanocomposites, metal deposited Mn-based oxides etc., display superior electrochemical performance. For example, MnO_x combined with a variety of elements (e.g., Pt, Pd, Ni, Mg, Ca) have been already reported to exhibit superior catalytic activity than both pristine metals.[19,20] Bimetallic nanoparticle like Au–Pd supported on MnO_2 catalysts have been reported with better catalytic activity for ORR and OER. Moreover, Mn-based oxides like spinel $Co_xMn_{3-x}O_4$, and perovskite $CaMnO_3$ along with various nanostructures have also been reported to exhibit high catalytic activity both in ORR and OER of the metal–air batteries.[19,20] Therefore, Mn-based mixed oxides catalysts could exhibit sustainable prospects for bifunctional electrocatalytic activity. Having MnO_2 as one of the best ORR catalyst, the next task would be to find appropriate OER catalyst to make Mn-based bifunctional mixed oxides catalyst.

Due to the unique characteristics such as high metallic conductivity, catalytic activity and the electrochemical redox properties, ruthenium–based nanoparticles catalysts have been actively explored in various chemical and electrochemical oxidation reactions.[21–26] Byon et al.[27] reported the improved performance of lithium air batteries by the dispersion of RuO_2 nanoparticles on carbon nanotube (CNT). The battery showed a high round–trip efficiency (ca. 79%), with discharge and charge overpotential of 0.21 and 0.51 V, respectively. This excellent performance was ascribed to the RuO_2 layer coated on the CNTs which effectively prevented direct contact between the CNTs and the discharge products Li_2O_2, and thus prevent/reduce the formation of insoluble solid side products which might induce large polarization or charge failure. Wang et al.[28] explored Ru nanocrystals as OER catalyst for Li-O_2 batteries and reported lowest charge-discharge over potential of about 0.37 V. Similar results were also reported by Shao–Horn et al.[29] according to which the hydrous RuO_2 nanoparticles of ∼6 nm exhibited excellent OER activities in both acidic and alkaline solutions, as well as better stability. While α-MnO_2 is most active for ORR, RuO_2 seems to be most active for OER. So in this study, the main idea is to combine both α-MnO_2 and RuO_2 catalysts as bifunctional catalyst for air cathode.

As mentioned earlier, both optimization of composition and morphology control of the catalysts are necessary to enhance the electrocatalytic activity. So we design a 3 dimensional (3D) nanostructured bifunctional catalyst. The 3D nanostructure might be able to provide large surface area and large pores to facilitate the gas–phase oxygen and liquid–phase electrolyte diffusions. 3D structure can also accommodate the reversible formation and decomposition of insoluble discharge products, reduce the diffusion resistance of oxygen and

*Electrochemical Society Active Member.
[z]E-mail: nahmks@jbnu.ac.kr; leeys@chonnam.ac.kr

electrolyte, enhance the ion transportation and maintain very smooth electron pathways in the charge/discharge reactions. In this point of view, mixed oxides (manganese oxide and ruthenium oxide) 3D structure is a suitable option to be bifunctional electrocatalysts in the air cathode.

In this work, therefore, we have synthesized unique 3D nanostructure of sea urchin shaped α–MnO_2 and RuO_2 mixed oxides by simple low temperature hydrothermal technique. The unique nanostructured mixed oxides are expected to provide large surface area and excellent accessibility to the reactive species as well as possess relatively high catalytic activities for both ORR and OER. Even though this combination has been investigated for various purposes, to the best of our knowledge, this is the first report on the synthesis of sea urchin shaped α–MnO_2/RuO_2 nanostructure. This work mainly focuses on the investigation of the catalytic performance of the α–MnO_2/RuO_2 nanostructure to address the overpotential issues of the OER reaction in Li-O_2 cells. We demonstrate urchin shaped mixed oxides with unique combination of MnO_2 support and Ru–based nanocrystals which exhibit superior bifunctional catalytic activity and reduces the overpotential. The synthesized catalyst is found to be better than only α–MnO_2 and the commercial Pt/C.

Experimental

Synthesis of RuO_2/α–MnO_2 mixed oxides.— α–MnO_2/RuO_2 mixed oxides was synthesized in the ratio of 82 : 18 using hydrothermal method. All chemicals (Sigma–Aldrich) were of analytical grade and used as received without further purification. The detail description of the synthetic process is given in our previous report.[13] To prepare α–MnO_2/RuO_2 (82 wt% α–MnO_2 /18 wt% RuO_2) mixed oxides, 0.34 g $MnSO_4.H_2O$, 0.54 g of $K_2S_2O_8$, 2 mL of H_2SO_4 and 0.078 g of $RuCl_2.H_2O$ were added into 40 ml of deionized water under stirring condition for 30 minutes. Then the mixed solution was transferred to Teflon–lined stainless steel autoclave and kept in a preheated electric oven at 110°C for 6 hours. The autoclave was then cooled down to room temperature and the brown precipitate was obtained. The product was centrifuged and washed with deionized water several times and then dried at 60°C for 8 hours in air.

Structure characterization.— The phase structures of the as–prepared sample was determined by powder x–ray diffraction, (XRD, Shimadzu XRD-6000) using a CuKα (λ = 1.54059 Å) target in the 2θ range of 10∼100°. The morphology of as–prepared sample was examined with field emission scanning electron microscopy (FESEM, JSM–6700F) and high resolution transmission electron microscopy (HRTEM, JEM–2010, JEOL). The chemical composition of the sample was investigated with inductively coupled plasma mass spectrometer (ICP-MS, Agilent 7500a, Agilent Technologies). Also x–ray photoelectron spectroscopy (XPS) was utilized to study the chemical composition of the synthesized sample. XPS analysis was performed with a thermo scientific Kα x–ray source. The Brunauer–Emmett–Teller (BET) technique was used to characterize specific surface area. The BET surface areas analysis of the carbon materials was obtained using a nitrogen adsorption instrument (BEL SORP Bell Japan Inc.). All the samples were degassed for 3 h at 300°C under vacuum before surface area measurements.

Lithium air battery studies.— For lithium air battery studies, the air cathodes were prepared by mixing as–prepared α–MnO_2/RuO_2 mixed oxides and Ketjen black (EC 600 JD) conductive carbon in the weight ratio of 1:2 with teflonized acetylene black (TAB) binder (60%) in isopropyl alcohol. The mixture was prepared into a fine pellet of about 1 cm diameter and the pellet was pressed on a Ni mesh current collector with a diameter of 1.2 cm. Thus prepared electrode was then dried in vacuum overnight at 100°C and used as air cathode in Li air battery. Lithium air battery performance was studied in a Swagelok type cell fabricated with the prepared air cathode, Li metal anode, and LiTFSI (TEGDME) (1:1) electrolyte. The Swagelok type cell was assembled in argon filled glove box under room temperature and purged with oxygen before cycle performance. The charge–discharge profiles of the cells were measured using BTS 2000 (Japan) system under 1 atm O_2 atmosphere.

Electrochemical characterization.— Electrocatalytic activity of the sample was evaluated by measuring oxygen reduction reaction (ORR) and oxygen evolution reaction (OER) polarization curves. The electrochemical studies were carried out using a computer controlled potentiostat (CHI 760D, CH Instrument) equipped with a typical three electrode cell. In the test cell, Pt wire and Hg/HgO were used as the counter and reference electrodes, respectively. Prior to the electrochemical measurement, O_2 was bubbled directly into the cell for at least an hour.

To prepare a working electrode for electrochemical studies, the as–synthesized sample was mixed with carbon powder (Cabot Vulcan XC-72) in the weight ratio of 3:7 to ensure sufficient electronic conductivity. 10 mg of the mixture was dispersed ultrasonically in 150μL of diluted nafion alcohol solution (5 wt%) dissolved in isopropyl alcohol (IPA), and about 13.5 μL of the suspension was pipetted onto a glassy carbon substrate. The linear sweep voltammetry (LSV) employed a rotating ring glassy carbon disk electrode (RRDE, 5.61 mm in diameter) for the glassy carbon substrate. To measure the ORR and OER polarization curves, the LSV were recorded in the oxygen saturated 0.1 M KOH solution at a scan rate of 5 m s^{-1} with a disk rotation rate of 1600 rpm. The ORR and OER polarization curves were obtained in the potential ranges of 0.3 ∼ −0.8 V and 0.3 ∼ 1.0 V, respectively.

Results and Discussion

Structural characterization.— Figure 1a shows the XRD spectrum, (b) nitrogen adsorption–desorption isotherms and (c) ICP analysis, for α–MnO_2/RuO_2 mixed oxides. All the XRD peaks can be indexed to two phases of α–MnO_2 tetragonal crystalline (I4/m space group) and tetragonal RuO_2.The lattice constants of α–MnO_2 and RuO_2 were calculated from the XRD spectrum (Fig. 1a) using Rietvald method and are found to be a = b = 9.83°A and c = 2.87°A; and a = b = 4.50°A, c = 3.12°A, for α–MnO_2 and RuO_2, respectively. These values are in very good agreement with the data given in JCPDS cards (JCPDS 44–0141 and JCPDS 40–1290).[13,30] Peaks located at 2 θ = 18, 28, 37, 57, 61 and 69 correspond to the (200), (310), (211), (600), (521) and (541) planes of α–MnO_2, while the peaks appeared at 2 θ = 27, 35, 54, 58 and 67 represent the (110), (101), (211), (220) and (112) planes of RuO_2. The high intensity of the peaks at 2 θ = 28° (310) and 37° (211) shows the crystallinity of the synthesized oxides. XRD pattern in Fig. 1a shows the very defining peak positions of the metal oxides, α–MnO_2 and RuO_2, which indicates that the synthesized mixed–oxides are composed of homogeneously distributed MnO_2 and RuO_2 nanoparticles. The crystal size of the sample was calculated using the Scherrer equation 1 as given below with peaks at 2 θ = 28° and 12° for RuO_2 and α–MnO_2, respectively.[31] The mean crystal sizes of RuO_2 and α–MnO_2 are about 15 and 29 nm, respectively.

$$D_{hkl} = \frac{0.89\lambda}{\beta\,(2\theta)\cos(\theta)} \quad [1]$$

Table I shows the BET specific surface area of the synthesized α–MnO_2/RuO_2 mixed oxide to be 53.10 m^2 g^{-1} which is slightly higher than α–MnO_2 urchin (50 m^2 g^{-1}). The desorption–adsorption isotherm is very useful to find out the porosity and the type of isotherm of the sample. As it can be seen in Fig. 1b the isotherm of the mixed oxide exhibits the characteristics of type IV, and the hysteresis loop is an indicative of mesoporosity. The closure at P/P_o ∼0.45 indicates the presence of small mesopores. There is a vertical shift in the location of hysteresis loop to higher volumes of nitrogen gas adsorption, indicating the enhanced porosity in the sample. It is believed that these mesopores can deliver a shorter ion transport pathway and more triple–phase (solid–liquid–gas phases) regions required for oxygen reduction. The pore size distribution was derived using the BJH

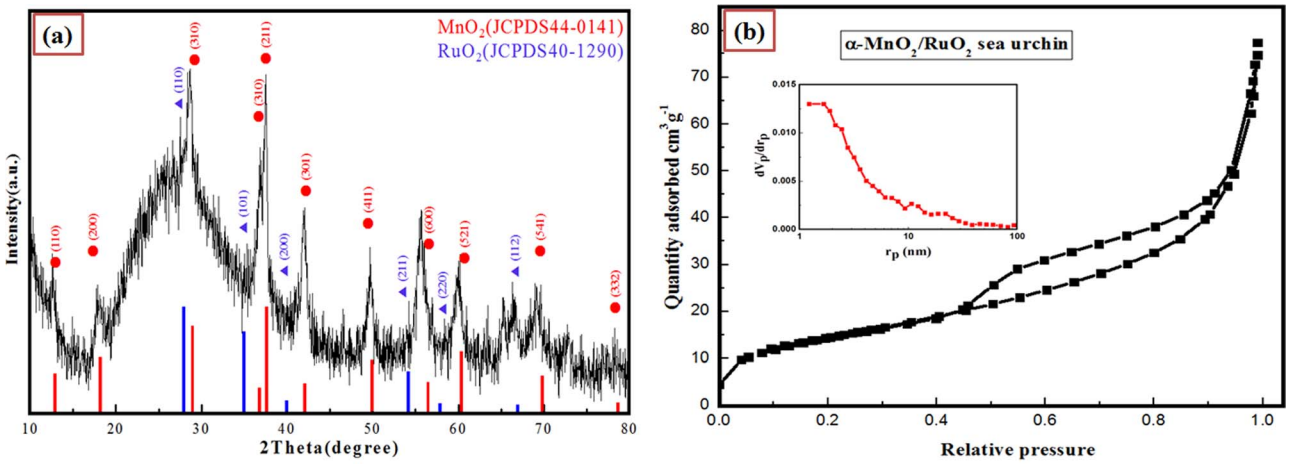

(c) Elemental analysis ICP-MS

Element	ICP-MS (wt.%)	Theoretical value (wt.%)
O	40.8	35.59
Ru	11.1	13.45
Mn	48.1	50.96

Figure 1. (a) XRD spectrum, (b) nitrogen adsorption–desorption isotherms and (c) ICP analysis for α–MnO_2/RuO_2 mixed oxides.

(Barrett–Joyner–Halenda) method. Pore size distribution pattern of the mixed oxide was illustrated from the nitrogen theoretical database and its corresponding experimental data is shown in inset of Fig. 1b. The pore size distribution curve shows that the pore size is scattered between 10–12 nm. The average pore diameter of the mixed oxide is found to be 9–10 nm.

In order to confirm the composition of manganese, ruthenium and oxygen in the synthesized mixed oxides, the inductively coupled plasma mass spectrometry analysis was performed and given in Figure 1(c). The ICP measurement for the synthesized MnO_2/RuO_2 mixed oxides shows that our synthesized mixed oxides are composed of 48.wt% of Mn, 11 wt% of Ru and 40.8 wt% of oxygen. These values are almost comparable to those of the stoichiometric weight percent of Mn, Ru and O in our synthesized MnO_2/RuO_2 mixed oxides which are 50.9, 13.4 and 35.5 wt%, respectively.

The morphology of the synthesized α–MnO_2/RuO_2nanostructure was examined by FESEM, transmission electron microscope (TEM), selected area electron diffraction (SAED) and TEM energy dispersion spectroscopy (EDS) mapping analyses and their results are summarized in Figure 2. Figure 2b shows the morphology of the α–MnO_2/RuO_2mixed oxides. The α–MnO_2/RuO_2mixed oxides are formed like sea urchin–shaped nanostructures with 2.5–3.0 μm diameter, which consists of several straight and radially grown nanorods with uniform diameter of 50 nm. For comparison, FESEM image of pure α–MnO_2 is also given in Fig. 2a. The FESEM image clearly shows the formation of α–MnO_2 sea urchin–shaped nanostructures with 2–2.5 μm diameter. It is seen that the diameter of the sea urchin–shaped nanostructures slightly increases with the addition of RuO_2 to α–MnO_2. Although (not shown in this manuscript), it was observed that with the increase of ruthenium oxide content in the nanostructure, not only the roughness of the sea urchin was increased but also the diameter of the nanorods originating from urchin increased approximately from 30 to 50 nm. The TEM images in Fig. 2c of α–MnO_2/RuO_2 clearly show the formation of nanourchins by the radially aligned nanorods. Furthermore, the detailed structural information was provided by the apparent lattice fringes of α–MnO_2/RuO_2. HRTEM image of Fig. 2d, reveals the interlayer spacing of 0.48 nm and 0.32 nm, confirming the distance of (200) planes of α–MnO_2 and (111) planes of RuO_2, respectively. From HRTEM analysis and SAED pattern (inset of Fig. 2d), it is clear that the preferential growth direction of the α–MnO_2/RuO_2 nanostructure was along the (200) direction. The TEM results are quite consistent with the XRD pattern which shows the successful formation of α–MnO_2/RuO_2 mixed oxide nanourchins. In order to identify the homogeneous distribution of RuO_2 and MnO_2 in the α–MnO_2/RuO_2 sea urchin–shaped nanostructures, the TEM–EDS analyses were performed as shown in the Figure 2e–(h). The mapping of each element shows uniform distribution of Mn, Ru, and O throughout the sea urchin nanostructures. This clearly confirms the homogenous distribution of RuO_2 and MnO_2in the mixed oxide.

For in–depth chemical composition analysis of α–MnO_2/RuO_2 sea urchin, XPS analysis was performed and the spectra are as shown in Fig. 2i–2k. XPS survey clearly indicates the existence of manganese, ruthenium and oxygen in the nanostructure (Figure 2i). From

Table I. BET data and ORR– OER properties of the samples.

		For ORR		For OER	
Sample	Specific surface area m^2 g^{-1}	Onset Potential V	Limiting Current mA	Onset Potential V	Limiting Current mA
α-MnO_2 (Urchin)	50.19	−0.11	0.77	0.65	−0.95
α-MnO_2/RuO_2 (Urchin)	53.10	−0.03	0.87	0.60	−3.0
Commercial RuO_2	8.06	−0.15	0.67	0.66	−1.81
Commercial 30 wt% Pt/C	160*	−0.03	0.9	0.78	−2.22

*Value obtained from Premetek Company

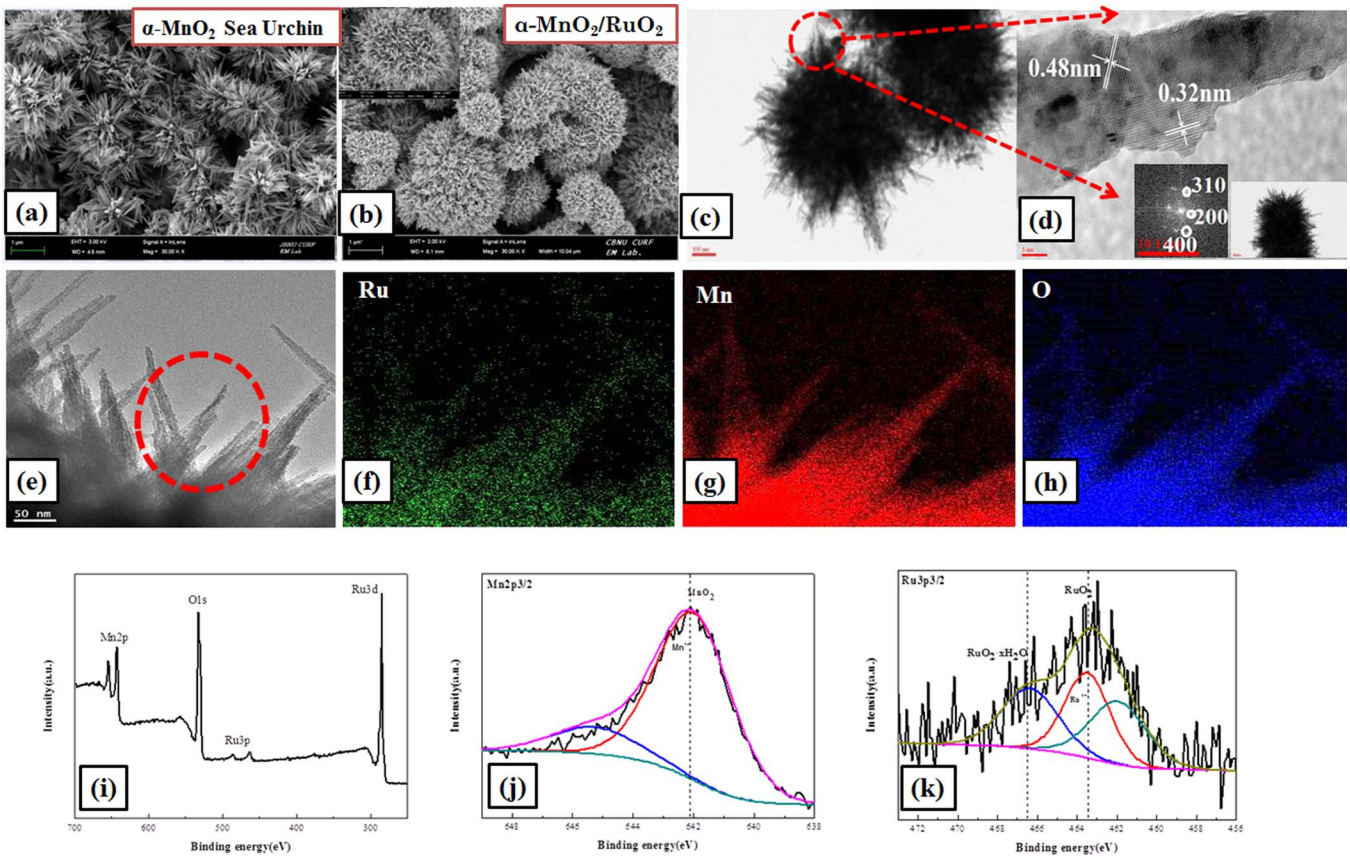

Figure 2. (a, b) FESEM images; (c, d) TEM images (SAED pattern-inset image of d); (e–h) TEM–EDS mapping, and (i–k) XPS spectra of α–MnO_2/RuO_2 mixed oxides.

Mn 2p3/2 spectrum (Figure 2j), the main peak located at 642.2 and 645 eV can be assigned to Mn (IV) from MnO_2.[32,33] Fig. 2k shows the high resolution scans of the Ru 3p region for α-MnO_2/RuO_2 sea urchin. The deconvolution of the Ru 3p region of RuO_2 nanoparticles shows the presence of Ru and RuO_2 components.[34] The Ru 3p3/2 signal could be deconvoluted into two peaks at 463.8 and 466.5 eV, respectively. A main peak centered at 463.8 eV can be assigned to Ru (IV) oxide (RuO_2).[35,36] The peak centered at 466.5 eV can be assigned to $R_uO_2 \cdot xH_2O$. From XPS spectra, the major chemical composition for the mixed oxide nanostructure was found to be composed of fully oxidized Ru^{4+} and Mn^{4+} states, which also confirmed that the final composition of the sea urchin structures was α–MnO_2/RuO_2. Consequently, all the above mentioned experiments clearly identifies that the synthesized α–MnO_2/RuO_2 sea urchin nanostructure is composed of homogeneously distributed MnO_2 and RuO_2 nanoparticles.

Lithium air battery characteristics.— The Li–O_2 battery was constructed using the synthesized α–MnO_2/RuO_2 nanostructure catalyst, and the charge–discharge performance of the batteries was evaluated in Swagelok type cells. Figure 3a shows the charge–discharge curves of Li–O_2 battery measured at 0.1 mA cm^{-2}. The α–MnO_2/RuO_2 exhibits rather stable specific capacities of about 3500–5500 mAh g^{-1} with low overpotential even after three cycles. The first two cycles exhibit 95% capacity retention on charging. On the contrary, the discharge capacity of the only KB electrode without any catalyst decreases dramatically down to 1095 mAh g^{-1} after three cycles (Fig. 3a). It is worthwhile to notice the difference in overpotential between α–MnO_2/RuO_2 catalyzed cell and KB cell as well. The better result might be attributed to the unique properties of the electrode such as porosity and nanostructure as well as chemical reactivity of the α–MnO_2/RuO_2 catalyst, which facilitate the favorable formation and decomposition of the discharge product and improve the reversibility of the O_2 electrode.

In the charge-discharge curves, the discharge curves show stable plateaus and the charging curves slopes without any apparent plateaus. Generally, Li_2O_2 formed during discharge process decomposes into 2Li and O_2 on charging process. In our case, the main discharge product Li_2O_2 is formed on discharge which can be confirmed from XRD (Fig. 5a). However additional by-product LiOH is also observed in the XRD spectra. Recently Wang et al. also reported similar type of charge-discharge curves.[28] According to the authors, the formation of LiOH is due to the reaction of Li_2O_2 with the structural water content in Mn–Ru oxides. There were no other side products observed. During the discharge the electrode surface should have been covered with the discharge products. According to Wang et al.,[28] the first low charge plateau is associated with the decomposition of Li_2O_2 whereas the second higher plateau from 3.5 V might be associated with the decomposition of the by-products, in this case LiOH. Nevertheless, the charge plateau for the MnO_2/RuO_2 catalyst seems to be lower than the Li-air cell without any catalyst owing to their catalytic activity.

Inspired by the enhanced performance of the electrocatalyst in capacity retention and suppressing the overpotential, we further examined the efficiency of the catalyst on the rate performance of Li–O_2 cells at different current densities. It can be seen that the Li–O_2 cells with α–MnO_2/RuO_2 electrodes exerts stable and high discharge capacity (Fig. 3b) under all investigated current densities (0.1, 0.2 and 0.3 mA cm^{-2}). This enhanced rate capability could also be reasonably attributed to the synergistic effect of the catalytic activity and unique urchin structure of the α–MnO_2/RuO_2 catalysts.

To obtain complete stable cycling without any fade in the capacity we also investigated the cell with a limited depth of discharge. Considerable cycling performance can be improved by limiting the depth of discharge.[37,38] The cycle life and efficiency of the battery were analyzed with a fixed capacity of 500 mAh g^{-1} at 0.1 mA cm^{-2}, as given in Fig. 3c. The cycling data shows a uniform

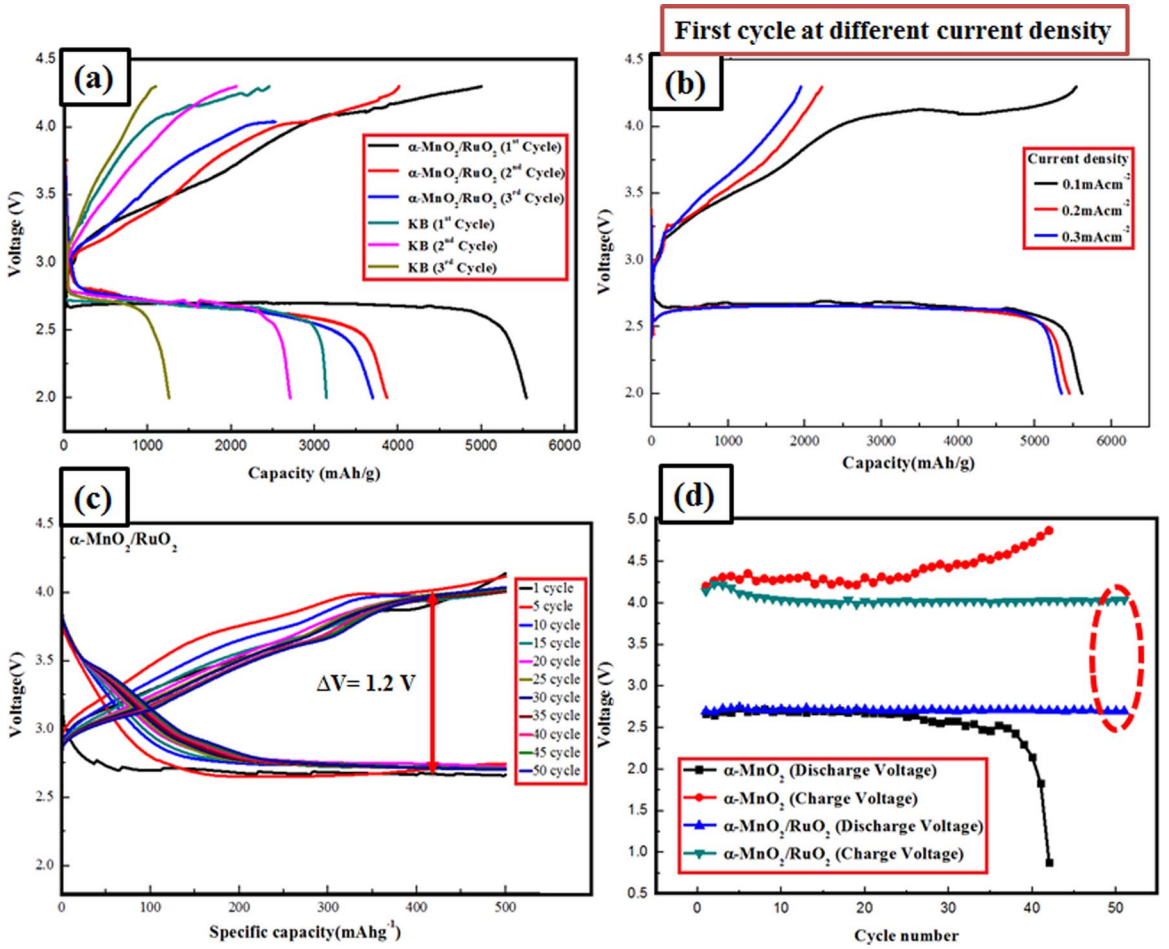

Figure 3. The charge–discharge curves of α–MnO_2/RuO_2 catalyzed Li–O_2 battery measured at (a) 0.1 mA cm^{-2}, (b) at different current densities, (c) with limited depth of discharge, and (d) charge–discharge potentials as a function of cycle number.

discharge–charge up to 50 cycles with low over potential. Generally the charge overpotential slowly increases during prolonged cycling and the capacity slowly fades. But in this case even after 50 cycles the charge potential is maintained at 4 V with overpotential of 1∼1.2 V maintained throughout the cycling. In other words, there was no significant increase in charge potential upon cycling. Therefore even after 50 cycles, the cycling profile with 500 mAh g^{-1} maintains steady round trip efficiency.

We extracted charge and discharge potentials from Fig. 3c and plotted them as a function of cycle number in Fig. 3d. For comparison, the overpotential of the α–MnO_2 catalyst was also gathered from charge and discharge curves measured with a limited depth of discharge (500 mAh g^{-1} at 0.1 mA cm^{-2}). As it can be seen from Fig. 3d, the α–MnO_2/RuO_2 catalyst is highly stable up to 50 cycles and there is no significant change in overpotential. But it is seen that the α–MnO_2 urchin nanostructure is stable only up to 25 cycles with increasing overpotential during discharge and charge process. The results clearly indicate that the α–MnO_2/RuO_2 catalyst outperforms the α–MnO_2 catalyst with its cycle life and rate capability. This enhanced cycle properties could be attributed to the unique combination of MnO_2 and RuO_2 in sea urchin nanostructure.

From the cell test of the lithium air battery using the α–MnO_2/RuO_2 nanostructure it can be seen that the α–MnO_2/RuO_2 exhibits rather stable specific capacities with low overpotential and good capacity retention even at higher current densities.

Electrochemical behavior of α-MnO_2/RuO_2 sea urchin nanostructures.— In order to see why the lithium air battery with α–MnO_2/RuO_2 nanostructure catalyst exhibit better battery performance, we investigated the electrochemical properties of the α–MnO_2/RuO_2 nanostructure for ORR and OER in KOH aqueous solution. LSV was employed to study the electrocatalytic activity of the synthesized α–MnO_2/RuO_2 nanostructure toward ORR. LSV was measured in a cathodic reduction region (0.3 ∼ −0.8 V vs. Hg/HgO) in O_2 saturated 0.1 M KOH at a scan rate of 5 mV s^{-1} with the electrode rotation rate of 1600 rpm, as shown in Fig. 4. The catalytic activity of a catalyst to the reaction could be qualitatively estimated from the onset potential and limiting current measured in LSVs. For comparison, ORR was also performed on α–MnO_2, commercial 30 wt% Pt/C and RuO_2 under the same analytic conditions. For each of the investigated materials, the measured onset potentials and limiting currents for ORR are summarized in Table I. The onset potential of α–MnO_2/RuO_2 is −0.03, which is more positive than α–MnO_2 and commercial RuO_2, respectively. Similar results have been observed for the limiting current of α–MnO_2/RuO_2 catalyst, which is significantly higher than α–MnO_2 urchin and the commercial RuO_2. Although the onset potential and limiting current of α–MnO_2/RuO_2 sample are little lower than commercial Pt/C, the significant positive shift of onset potential and the higher values of limiting current in α-MnO_2/RuO_2 in comparison with α–MnO_2 and commercial RuO_2 explicitly shows that the α–MnO_2/RuO_2 urchin nanostructure is catalytically more active. The overall electrochemical reaction of the lithium–air battery can be expressed as,

$$2(Li^+ + e^-) + O_2 \rightleftarrows Li_2O_2 \quad [2]$$

during which ORR takes place on discharge process (forward reaction), followed by OER on charging (reverse reaction). In order to

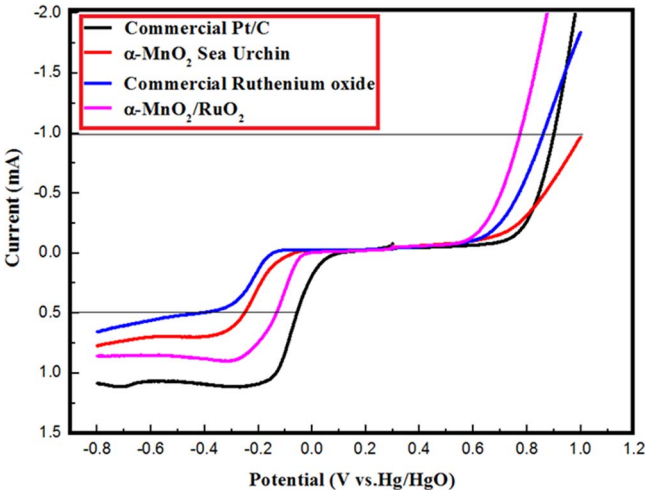

Figure 4. LSV curves measured in the cathodic reduction region (−0.8∼0.3 V vs. Hg/HgO) and anodic potential up to 1.0 V vs. Hg/HgO in O_2 saturated 0.1 M KOH at a scan rate of 5 mV s^{-1} and 1600 rpm for ORR and OER.

attain higher battery performance, both the ORR and OER need to progress as rapid as they can. Various electrochemical evaluations have proven that the α–MnO_2/RuO_2 nanostructure is one of the most active catalysts for the ORR. Therefore we examined whether the α–MnO_2/RuO_2 nanostructure is also an effective catalyst for the decomposition of the discharge product, Li_2O_2.

The synthesized MnO_2/RuO_2 nanostructure exhibits superior performance in OER than all other samples including commercial Pt/C. To evaluate the ability to catalyze OER, we measured the polarization curves on the LSV during the anodic potential scan up to 1.0 V vs. Hg/HgO as shown in Figure 4. The measurements were recorded in O_2 saturated 0.1 M KOH at a scan rate of 5 mV s^{-1} with the electrode rotation rate of 1600 rpm. Again, for comparison, OER was also performed on α–MnO_2, commercial 30 wt% Pt/C and RuO_2 under the same analytic conditions. Interestingly, the synthesized MnO_2/RuO_2 nanostructure exhibits a superior performance in OER than all other samples including commercial Pt/C. That is, the α–MnO_2/RuO_2nanostructure exhibits lower onset potential and higher limiting current than those of commercial Pt/C and Ru/C which displays its bifunctional catalytic behavior. The onset potential of the electrode with α–MnO_2/RuO_2 catalyst is 0.60 V, which is lower than the electrode prepared with commercial Pt/C and RuO_2, respectively. This identifies that the α–MnO_2/RuO_2nanostructure is an excellent OER catalyst which can be employed as a promising bifunctional catalyst in the air cathode of Li–O_2 battery.

In order to identify that the α–MnO_2/RuO_2 nanostructure is also an excellent OER catalyst in the Li–O_2 battery, we examined and compared the catalytic activities of Li_2O_2 decomposition over the catalysts using Swagelok type cells. The discharge-charge cycling was carried out over air cathode (i) without any catalyst, (ii) with Pt/C catalyst and (iii) our synthesized α-MnO_2/RuO_2 mixed oxide catalyst. The surface composition and morphology of the air electrodes were investigated before and after discharge and charge processes using XRD and SEM, respectively. Figure 5a shows the XRD spectra which were measured before and after discharge/charge during the first cycle for air cathodes (i) without any catalyst, (ii) with Pt/C catalyst and (iii) our synthesized α-MnO_2/RuO_2 mixed oxide catalyst. A broad carbon (2 θ = 23°, 44°), TAB (2θ = 17°), and Ni (2θ = 43.5°, 47.6° and 51°) peaks are observed from all the XRD spectra. For air cathode (i) without any catalyst, the XRD spectrum before discharge cycling shows characteristic peaks for KB without any other impurity. After the first discharge, the XRD peaks shows the formation of Li_2O_2 at 2θ = 32°, 35° and 58° as discharge product. It is clearly seen that, the same Li_2O_2 peaks remain on the electrode surface even after charging process as observed after the discharge, indicating the poor decomposition of Li_2O_2. For the Pt/C catalyzed cathode (ii), the XRD spectrum before discharge shows characteristic peaks for Pt and carbon without any other impurity. After the first discharge, the XRD peaks clearly shows the formation of Li_2O_2 at 2θ = 32°, 35° and 58°. After charging, it exhibits weak intensities of the Li_2O_2 peaks, indicating the remaing of partially non-decomposed Li_2O_2. In the case of the α-MnO_2/RuO_2 mixed oxide catalyzed air cathode (iii), α-MnO_2 and RuO_2 related peaks are observed in the XRD spectrum before discharge. For reference, the inset Fig. 5a gives the JCPDS files of α-MnO_2 and RuO_2.[30] After discharge, the XRD peaks clearly shows the formation of Li_2O_2 at 2θ = 2θ = 32°, 35° and 58° with a trace of LiOH at 2θ = 32.4° and 35.6°. Interestingly, after charging the Li_2O_2 peaks are completely disappeared from the XRD spectrum, indicating the complete decomposition of Li_2O_2. Thus from Figure 5a , it is clear that our synthesized α-MnO_2/RuO_2 mixed oxide catalyst is better than Pt/C catalyst for the decomposition of Li_2O_2 on the air cathode.

Figure 5b shows the SEM images which were taken before and after discharge/charge during the first cycle for air cathodes (i) without any

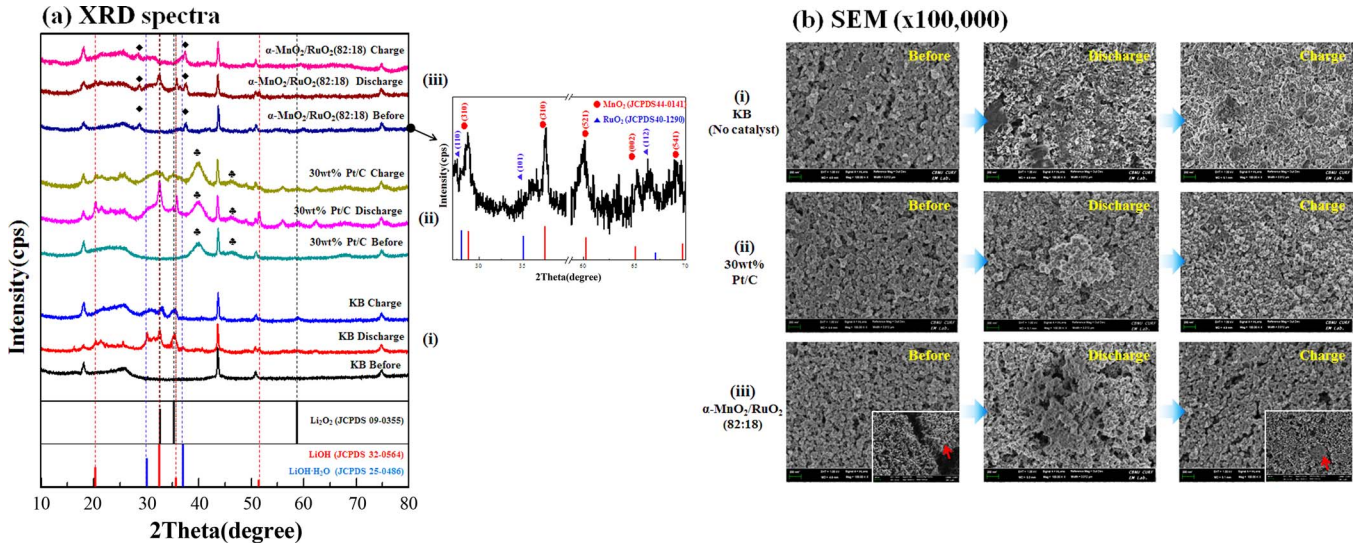

Figure 5. (a) XRD spectra and (b) SEM images of air cathodes (i) without any catalyst, (ii) with Pt/C catalyst and (iii) our synthesized α-MnO_2/RuO_2 mixed oxide catalyst measured before and after discharge/charge.

Table II. Electrochemical properties of the catalysts.

	ORR E(V) at I = 0.5 mA		OER E(V) at I = −1.0 mA		Oxygen Electrode
	Onset Potential V	Limiting Current mA	Onset Potential V	Limiting Current mA	Δ (OER-ORR) E(V)
α-MnO_2 (Urchin)	−0.11	0.77	0.67	−0.95	1.23
α-MnO_2/RuO_2 (Urchin)	−0.03	0.87	0.57	−2.98	0.90
Commercial RuO_2	−0.15	0.65	0.60	−1.81	1.23
Commercial Pt/C	0.02	1.09	0.70	−2.22	0.95

catalyst, (ii) with Pt/C catalyst and (iii) our synthesized α-MnO_2/RuO_2 mixed oxide catalyst. From the SEM images taken before discharge, it can be seen that all the air cathodes (i) without any catalyst; (ii) with Pt/C catalyst and (iii) our synthesized α-MnO_2/RuO_2 mixed oxide catalyst shows a smooth surface with not much noticeable differences. After the first discharge, the air cathode without any catalyst (i) shows agglomerations all over the cathode surface which indicates the formation of Li_2O_2 (see Fig. 5b). The air cathodes with Pt/C and α-MnO_2/RuO_2 mixed oxide catalyst also shows the formation of agglomerations on the cathode surface though the configuration of the agglomeration is slightly different. After charging, however, quite different surface morphologies are observed from the electrode surfaces with and without catalysts. The air cathode (i) without any catalyst shows almost similar agglomeration to remains, indicating only poor decomposition of Li_2O_2. But the air cathode with Pt/C exhibits scattered agglomerations over the cathode surface, indicating the residue of partially non-decomposed Li_2O_2. It is interesting to see that the air cathode with α-MnO_2/RuO_2 mixed oxide catalyst presents almost similar cathode surface to that of the original one before discharge/charge cycle indicating the almost complete decomposition of Li_2O_2. This explains that the α-MnO_2/RuO_2 mixed oxide is an effective OER catalyst for the decomposition of solid discharge product Li_2O_2.

This is in perfect agreement with Fig 3a and 5a proving that our synthesized MnO_2/RuO_2 mixed catalyst is better than the other catalysts for both ORR and OER promoting complete decomposition of Li_2O_2.

To assess the overall oxygen electrode activity, the potential difference between the ORR and the OER curves were calculated and the details are summarized in Table II. Table II quantitatively compares the bifunctional oxygen electrode activity of the α–MnO_2/RuO_2 with those of the α–MnO_2 urchin, commercial Pt/C and RuO_2. Figure 4 is used to quantify the ORR and OER for the materials. The potential at which the current reaches the half of its maximum value (half–wave potential) was selected for the ORR activities of the samples. Therefore, in this case, ORR current of −0.5 mA was selected which approximates the half–wave potential. Activities for the OER were judged by the potential required to oxidize water at a current of −1.0 mA, a convention commonly used in the OER analysis.[39] The smaller the difference, the closer the catalyst is to an ideal reversible oxygen electrode. From Table II, it is seen that the mixed oxide α–MnO_2/RuO_2 catalyst has an oxygen electrode activity of 0.90 V, which is the least value among other catalyst used in this work. These results indicate that the mixed oxide sample is highly active both for ORR and OER, which is attributed to the unique 3D metal oxide catalyst and the uniform distribution of the particles throughout the urchin structure.

From structural and chemical characterizations, we conclude that the synthesized α–MnO_2/RuO_2 sea urchin nanostructure is composed of homogeneously distributed MnO_2 and RuO_2 nanoparticles. Based on the precursors used for the synthesis in the experiment, it is considered that both α–MnO_2 and RuO_2 are simultaneously formed with the chemical reaction equation suggested as follows:[30]

$$MnO_4^- + 3Ru^{3+} + 4H_2O = MnO_2 + 3RuO_2 + 8H^+ \quad [3]$$

The unique 3D mesoporous α–MnO_2/RuO_2 mixed oxide exhibit an outstanding performance in aqueous and non–aqueous electrolytes because of its 3D structure which provides fast mass transport and favorable triple–phase (solid–liquid–gas phase) region required for electro–catalysis.[31] Song et al.[17] reported the high reversibility of Li–air batteries using α–MnO_2 catalyst mainly associated with its unique mechanism for deposition of discharge products. They suggest that the fast Li ion transport and reversible formation/decomposition of discharge products are attributed to the α–MnO_2 nanowires and propose a strategy for achieving high–power Li–air batteries in combination with nano–architecture tailoring. Yilmaz et al.[27] demonstrated that ruthenium oxide nanoparticles (RuO_2 NPs)/CNT as a cathode which increase the electrical efficiency up to 73%. RuO_2 nanoparticles contribute to the formation of poorly crystallized lithium peroxide (Li_2O_2) during oxygen reduction reaction (ORR) and smoothly decomposed the Li_2O_2 at low potential upon oxygen evolution reaction (OER). This report shows the enhanced performance of ruthenium oxide in transforming the crystal structure and morphology of Li_2O_2, which results in a remarkable decrease of energy loss during the OER.

From the above, our experimental results prove that the α–MnO_2/RuO_2 catalysts can effectively facilitate both ORR and OER. The significantly decreased overpotential of the catalyst may also be ascribed to the much enhanced OER activity of the α-MnO_2/RuO_2 mixed oxide catalyst. α–MnO_2 is beneficial with its 2×2 crystal structure which favors the transfer of ions in addition to the OH^- groups which helps in surface adsorption of O_2 and dissociation of O–O bonds.[13] In addition, the use of RuO_2 provides several advantages including (i) the high electrical conductivity, (ii) the synergistic effect between the α–MnO_2 and the RuO_2, and (iii) the high carrier density and conductivity in comparison to other stoichiometric metal oxides. The improved cycleability probably relies on the better reversible formation and decomposition of Li_2O_2 occurring on electrocatalytic α–MnO_2/RuO_2 nanourchins during discharge and charge processes. RuO_2 is more active due to the weaker oxygen bonding than the chemisorbed oxygen on metallic Ru.[40] It has been shown that OER process for RuO_2 involves surface–adsorbed O, OH, and OOH intermediates.[41,42] It has also been reported that RuO_2 catalysts showed low OER overpotential mainly due to oxygen binding and hydroxyl binding surface forces.[29,30] The improved performance of the α–MnO_2/RuO_2 based cathode can be ascribed to two aspects. Firstly, it is the superior electrocatalytic behavior of α–MnO_2/RuO_2 toward both ORR and OER, which are afforded by its inherent electronic structure and favorable electronic transport capability as confirmed in both aqueous[32] and non–aqueous phase we have observed herein. Secondly, it is the homogenous distribution of both the metal oxides and the 3D structure of α–MnO_2/RuO_2, which also plays a crucial role in its electrochemical behavior. This interesting structure not only provides more electrocatalytic sites but also promotes mass transport (oxygen and ions) in the electrolyte, and eventually improves the capacity and cycleability of Li–O_2 cells.[43,44] Although the explicit mechanism to the significantly enhanced catalytic behavior of the nanostructure has not yet been fully understood, we ascertain that the α–MnO_2/RuO_2 mixed oxides can accelerate the kinetics of both the ORR and OER, which should be ascribed to the unique structural property. In view of the above considerations, additional works are certainly needed to confirm this interpretation.

Conclusions

In this work, we have synthesized sea urchin shaped α–MnO_2/RuO_2 mixed oxides nanostructure with a weight ratio of 82:18

via simple hydrothermal method. The α–MnO_2/RuO_2 mixed oxides nanostructure was formed with several straight and radially grown nanorods which are composed of homogeneously distributed MnO_2 and RuO_2 nanoparticles. The battery performance is remarkably improved because of the unique morphology of the α–MnO_2/RuO_2 mixed oxide catalyst. The Mn–Ru–based nanostructures have ability to catalyze ORR and OER with fast kinetics without electrolyte decomposition in Li–O_2 battery. We were able to find high ORR and OER activity for the synthesized α–MnO_2/RuO_2 nanostructure catalyst in both aqueous and non–aqueous electrolyte solutions. The bifunctional activity of the nanostructure catalyst is almost comparative to or much better than that of commercial Pt/C catalysts. Compared with α–MnO_2, the significantly improved catalytic activity for α–MnO_2/RuO_2 is probably due to their intrinsic property and can be attributed to the different O_2 adsorption kinetics and reaction pathway derived from the ruthenium oxide. This suggests that the synthesized catalysts could, in principle, overcome the limitation of Pt–based catalytic reaction systems and provide suitable, sustainable and cheap solutions for the further technological development of fuel cells and other oxygen electrodes.

Acknowledgment

This work was supported by the Human Resources Development program (No.20114030200060) of the Korea Institute of Energy Technology Evaluation and Planning (KETEP) grant funded by the Korea government Ministry of Trade, Industry and Energy. This research was also supported by Basic Science Research Program through National Research Foundation of Korea (NRF) funded by the Ministry of Education (2009–0094031).

References

1. P. G. Bruce, S. A. Freunberger, L. J. Hardwick, and J. M. Tarascon, *Nat. Mater.*, **11**, 19 (2012).
2. B. Scrosati and J. Garche, *J. Power Sources.*, **195**, 2419 (2010).
3. B. D. McCloskey, R. Scheffler, A. Speidel, G. Girishkumar, and A. C. Luntz, *J. Phys. Chem. C.*, **116**, 23897 (2012).
4. M. M. Ottakam Thotiyl, S. A. Freunberger, Z. Peng, and P. G. Bruce, *J. Am. Chem. Soc.*, **135**, 494 (2013).
5. T. Ogasawara, A. Débart, M. Holzapfel, P. Novak, and P. G. Bruce, *J. Am. Chem. Soc.*, **128**, 1390 (2006).
6. B. D. McCloskey, A. Speidel, R. Scheffler, D. C. Miller, V. Vishwanathan, J. S. Hummelshoj, J. K. Norskov, and A. C. Luntz, *J. Phys.Chem.Lett.*, **3**, 997 (2012).
7. Y. C. Lu, H. A. Gasteiger, and Y. S. Horn, *J. Am. Chem. Soc.*, **133**, 19048 (2011).
8. Y. Shao, S. Park, J. Xiao, J. G. Zhang, Y. Wang, and J. Liu, *ACS Catal.*, **2**, 844 (2012).
9. F. Cheng and J. Chen, *Chem. Soc. Rev.*, **41**, 2172 (2012).
10. E. Yoo and H. Zhou, *ACS Nano.* **5**(4), 3020 (2011).
11. R. R. Mitchell, B. M. Gallant, C. V. Thompson, and Y. S. Horn, *Energy Environ. Sci.*, **4**, 2952 (2011).
12. J. B. Park, J. Lee, C. S. Yoon, and Y. K. Sun, *ACS Appl. Mater. Interfaces.*, **5**, 13426 (2013).
13. A. Zahoor, H. S. Jang, J. S. Jeong, M. Christy, Y. J. Hwang, and K. S. Nahm, *RSC Adv.*, **4**, 8973 (2014).
14. W. Xiao, D. Wang, and X. W. Lou, *J. Phys.Chem.*, **114**, 1694 (2010).
15. Y. L. Cao, H. X. Yang, X. P. Ai, and L. F. Xiao, *J. Electroanalytical Chemistry.*, **557**, 127 (2003).
16. A. Débart, A. J. Paterson, J. Bao, and P. G. Bruce, *Angew. Chem. Int. Ed.*, **47**, 4521 (2008).
17. K. Song, J. Jung, Y. U. Heo, Y. C. Lee, K. Cho, and Y. M. Kang, *Phys. Chem. Chem. Phys.*, **15**, 20075 (2013).
18. F. Cheng, Y. Su, J. Liang, Z. Tao, and J. Chen, *Chem. Mater.*, **22**, 898 (2010).
19. K. Zhang, X. Han, Z. Hu, X. Zhang, Z. Tao, and J. Chen, *Chem. Soc. Rev.*,
20. Z. L. Wang, D. Xu, J. J. Xu, and X. B. Zhang, *Chem. Soc. Rev.*, **43**, 7746 (2014).
21. A. Zhang, C. B. Zhang, H. He, Y. B. Yu, L. A. Wang, and J. Zhang, *Chem. Mater.*, **22**, 4056 (2010).
22. D. R. Rolison, P. L. Hagans, K. E. Swider, and J. W. Long, *Langmuir.*, **15**, 774 (1999).
23. F. Li, J. Chen, Q. Zhang, and Y. Wang, *Green Chem.*, **10**, 553 (2008).
24. S. Wendt, A. P. Seitsonen, and H. Over, *Catal. Today.*, **85**, 167 (2003).
25. Y. D. Kim, H. Over, G. Krabbes, and G. Ertl, *Top. Catal.*, **14**, 95 (2001).
26. T. Reier, M. Oezaslan, and P. Strasser, *ACS catal.*, **2**, 1765 (2012).
27. E. Yilmaz, C. Yogi, K. Yamanaka, T. Ohta, and H. R. Byon, *Nano Lett.*, **13**, 4679 (2013).
28. B. Sun, P. Munroe, and G. Wang, *Scientific Reports.*, **3**, 2247 (2013).
29. Y. Lee, J. Suntivich, K. J. May, E. E. Perry, and Y. S. Horn, *J. Phys. Chem. Lett.*, **3**, 399 (2012).
30. K. Guo, Y. Li, J. Yang, Z. Zou, X. Xue, X. Lia, and H. Yang *J. Mater. Chem. A.*, **2**, 1509 (2014).
31. A. M. Benbow, S. P. Kelly, L. Zhao, J. W. Reutenauer, and S. L. Suib, *J. Phys. Chem. C.*, **115**, 22009 (2011).
32. K. C. Park, I. Y. Jang, W. Wongwiriyapan, S. Morimoto, Y. J. Kim, Y. C. Jung, T. Toya, and M. Endo, *J. Mater. Chem.*, **20**, 5345 (2010).
33. R. K. Tandon, R. Payling, B. E. Chenhall, P. T. Crisp, and J. Ellis, *Applications of Surface Science.*, **20**, 527 (1985).
34. Z. B. Wang, G. P. Yin, and Y. G. Lin, *J. Power Sources.*, **170**, 242 (2007).
35. Y. M. Liang, H. M. Zhang, H. X. Zhong, X. B. Zhu, Z. Q. Tian, D. Y. Xu, and B. L. Yi, *J. Catal.*, **238**, 468 (2006).
36. X. B. Fu, H. Yu, F. Peng, H. J. Wang, and Y. Qian, *Appl. Catal.,A: Gen.* **321**, 190 (2007).
37. R. Padbury and X. Zhang, *J. of Power Sources.*, **196**(10), 4436 (2011).
38. D. Xu, Z. l. Wang, J. J. Xu, L. L. Zhang, and X. B. Zhang, *Chem. Commun.*, **48**, 6948 (2012).
39. Y. Gorlin and T. F. Jaramillo, *J. Am. Chem. Soc.*, **132**, 13612 (2010).
40. X. Yang, X. Wei, C. Liu, and Y. Liu, *Materials Chemistry and Physics.*, **145**, 269 (2014).
41. J. Rossmeisl, Z. W. Qu, H. Zhu, G. J. Kroes, and J. K. Norskov, *J. Electroanal. Chem.*, **607**, 83 (2007).
42. J. Rossmeisl, A. Logadottir, and J. K. Norskov, *Chem. Phys.*, **319**, 178 (2005).
43. Y. M. Cui, Z. Y. Wen, X. Liang, Y. Lu, J. Jin, M. F. Wu, and W. Wu, *Energy Environ. Sci.*, **5**, 7893 (2012).
44. Y. L. Li, J. J. Wang, X. F. Li, D. S. Geng, M. N. Banis, Y. J. Tang, D. G. Wang, R. Y. Li, T. K. Sham, and X. L. Sun, *J. Mater. Chem.*, **22**, 20170 (2012).